Nanoscale Advances

ROYAL SOCIETY OF CHEMISTRY

PAPER

View Article Online
View Journal | View Issue



Cite this: *Nanoscale Adv.*, 2025, **7**, 7156

# Nitrogen-doped $Cu_4O_3$ thin films as high-performance counter electrodes for quantum dot-sensitized solar cells

Pham Minh Khang, [ab] Le Thanh Duy,[ab] Huu Phuc Dang [c] and Tran Le *[ab]

P-type metal oxide semiconductors are critical components in the development of next-generation optoelectronic and photovoltaic devices. While n-type materials such as $SnO_2$, ZnO, and ITO are well-established, the lack of stable, high-performance p-type transparent oxides with suitable bandgaps remains a key limitation. Among copper oxides, $Cu_4O_3$—a mixed-valence oxide—offers promising electronic and optical tunability, yet has been underexplored for device integration. In this work, nitrogen-doped $Cu_4O_3$ thin films were synthesized *via* DC magnetron sputtering under an (Ar + 10% $O_2$)/$N_2$ atmosphere. The incorporation of nitrogen effectively modulated the electronic structure, enhanced chemical stability, and improved electrical transport properties. The optimal film, denoted as $Cu_4O_3$-30 (30% $N_2$), exhibited a direct optical bandgap of 2.18 eV, resistivity of 4.19 Ω cm, hole concentration of $3.33 \times 10^{17}$ $cm^{-3}$, and hole mobility of 4.48 $cm^2$ $V^{-1}$ $s^{-1}$. When implemented as a counter electrode in $TiO_2$/CdS/CdSe:Cu/ZnS quantum dot-sensitized solar cells (QDSSCs), the device achieved a power conversion efficiency of 7.29%, exceeding the performance of its $Cu_2S$-based counterparts. These results highlight the potential of N-doped $Cu_4O_3$ as a scalable, chemically stable, and electrically efficient p-type oxide for emerging optoelectronic and photovoltaic technologies.

Received 8th July 2025
Accepted 10th September 2025

DOI: 10.1039/d5na00664c

rsc.li/nanoscale-advances



## 1. Introduction

Metal oxide thin films have long been integral to the advancement of photovoltaic technologies, owing to their favorable optical and electronic properties. Among these, wide bandgap n-type semiconductors such as $SnO_2$, ZnO, and indium tin oxide (ITO) are widely employed. These materials serve as transparent conductive layers, electron transport layers, or buffer layers in diverse device architectures, enabling efficient charge extraction and minimizing optical losses. However, next-generation optoelectronic devices—including solar cells, transparent transistors, and light-emitting diodes—demand not only efficient n-type materials but also transparent p-type layers with high hole conductivity and suitable band alignment. Such layers play a critical role in enhancing charge separation and transport under visible-light irradiation, thereby improving device performance.

Achieving stable p-type conductivity in metal oxides, however, remains a significant challenge. This challenge originates from intrinsic factors such as the deep nature of acceptor levels, self-compensation effects, and the strong localization of holes in O 2p orbitals, which collectively limit carrier mobility. In many cases, the difficulty in incorporating aliovalent dopants to create acceptor states is compounded by poor dopant solubility and low substitution efficiency—an issue noted in studies on p-type copper oxide films synthesized by ALD and sputtering methods.[1] Despite this, some metal oxides naturally exhibit p-type behavior, including SnO, NiO, and various copper oxides. Of these, SnO and NiO possess wide bandgaps (>3 eV), restricting their optical absorption in the visible range. In contrast, copper oxides, particularly those with narrower bandgaps and inherent p-type characteristics, offer strong potential for visible-light-driven optoelectronic applications.

Recent studies have drawn increasing attention to $Cu_4O_3$, a mixed-valence copper oxide comprising both Cu(I) and Cu(II) species. This compound inherits key features from $Cu_2O$ (direct bandgap ~1.82–2.56 eV)[2–7] and CuO (indirect bandgap ~1.42–2.07 eV),[8–12] resulting in tunable optical and electronic properties. Notably, $Cu_4O_3$ itself exhibits a direct bandgap ranging from 1.34 to 2.34 eV,[13–16] rendering it suitable for photoactive and photovoltaic applications. In addition to its optical versatility, the mixed-valence nature of $Cu_4O_3$ provides opportunities for defect engineering, particularly *via* aliovalent doping, to manipulate carrier concentration, mobility, and catalytic activity.

Copper-based oxides have been extensively explored for applications such as photocatalysis,[5] supercapacitors,[10] water splitting,[17] and light sensing,[9,18] with solar energy conversion

[a]*Faculty of Physics & Engineering Physics, VNUHCM – University of Science, Ho Chi Minh City 70000, Vietnam. E-mail: ltran@hcmus.edu.vn*

[b]*Vietnam National University Ho Chi Minh City, Ho Chi Minh City 70000, Vietnam*

[c]*Faculty of Fundamental Science, Industrial University of Ho Chi Minh City, Ho Chi Minh City, Vietnam*

receiving significant focus. Among these, $Cu_2O$ has emerged as a leading candidate due to its optimal bandgap and high absorption coefficient ($\sim 10^5$ $cm^{-1}$).[2–4,6,7,19–27] By contrast, $Cu_4O_3$ remains relatively underexplored. While several studies have demonstrated the synthesis of $Cu_4O_3$ films *via* DC[13,14,16] and RF sputtering,[15] and efforts have been made to tune its properties through thickness and phase engineering,[28] studies on dopant-induced electronic modification—particularly nitrogen doping—are rare. Nitrogen, with its comparable ionic radius to oxygen but distinct electronegativity, offers a potential route to substitute oxygen sites, introduce acceptor-like states, and tailor the electronic environment; however, such investigations for $Cu_4O_3$ are virtually absent. To date, only one report has addressed nitrogen incorporation in $Cu_4O_3$ *via* oxygen substitution.[15] Recent progress in QDSSC research has focused on interfacial engineering, advanced counter electrode design, and multifunctional quantum dot integration to enhance efficiency and stability.[29–31] Furthermore, no previous studies have evaluated $Cu_4O_3$ as a hole-conductive material in photovoltaic systems, particularly in quantum dot-sensitized solar cells (QdSSCs). This gap is critical because existing hole transport materials, such as $Cu_2S$, suffer from severe photocorrosion and instability, limiting their long-term device performance. This represents a critical knowledge gap. In this work, we address this void by synthesizing nitrogen-doped $Cu_4O_3$ thin films using DC magnetron sputtering under a mixed (Ar + 10% $O_2$)/$N_2$ atmosphere. We systematically investigate their structural, optical, and electrical properties and, for the first time, demonstrate their use as hole-transport layers in QdSSCs, replacing $Cu_2S$ in the traditional FTO/$TiO_2$/CdS/CdSe:Cu/ZnS/$Cu_2S$/FTO configuration.[32]

The N-doped $Cu_4O_3$ films display improved chemical stability, tunable electrical behavior, and enhanced catalytic robustness. These properties directly address the limitations of $Cu_2S$-based counter electrodes, which suffer from photocorrosion, chemical instability, and poor long-term performance.[33,34] By bridging the knowledge gap between fundamental defect engineering and device-level application, this study highlights the untapped potential of N-doped $Cu_4O_3$ as a scalable, stable, and efficient p-type layer for next-generation optoelectronic platforms.

## 2. Experiments

### 2.1. Fabrication of $Cu_4O_3$-*x* thin films

Nitrogen-doped copper oxide ($Cu_4O_3$-*x*) thin films were fabricated *via* direct current (DC) magnetron sputtering onto quartz and fluorine-doped tin oxide (FTO) substrates. Reactive sputtering was performed at a working pressure of $1 \times 10^{-3}$ torr in a mixed Ar + $O_2$ + $N_2$ atmosphere. The total gas flow rate was maintained at 50 sccm. The $O_2$ concentration was fixed at 10% of the total flow (*i.e.*, 5 sccm $O_2$), while the $N_2$ content was systematically varied from 0% to 40% of the total gas flow in 10% increments (*i.e.*, 0 to 20 sccm $N_2$). The balance of the flow (*i.e.*, 45–25 sccm) was Ar. For example, the 10% $N_2$ condition included 5 sccm $O_2$, 5 sccm $N_2$, and 40 sccm Ar; the 40% $N_2$ condition included 5 sccm $O_2$, 20 sccm $N_2$, and 25 sccm Ar. All gases (purity: 99.9999%) were introduced through high-precision mass flow controllers to ensure accurate control of the reactive gas composition. Prior to deposition, substrates were preheated to 150 °C to promote film adhesion and ensure uniform nucleation. High-purity (99.999%) copper targets with a 3-inch diameter and 0.25-inch thickness were utilized as the sputtering source. Film deposition was carried out in a Leybold Univex 450 high-vacuum system (Germany), where the chamber base pressure was maintained at $1 \times 10^{-6}$ torr. The sputtering power was fixed at 80 W, with the target-to-substrate distance set at 10 cm. Prior to deposition, both quartz and FTO substrates underwent sequential cleaning using deionized water, acetone, and a dilute NaOH solution to remove organic and ionic contaminants.

Fluorine-doped tin oxide (FTO) glass substrates (resistivity $\sim 7\ \Omega\ sq^{-1}$), titanium dioxide ($TiO_2$) nanoparticle paste (typically anatase phase, particle size ~20 nm), cadmium nitrate tetrahydrate ($Cd(NO_3)_2 \cdot 4H_2O$, ≥99%), sodium sulfide nonahydrate ($Na_2S \cdot 9H_2O$, ≥98%), selenium powder (Se, 99.99%), sodium borohydride ($NaBH_4$, ≥98%), copper(II) acetate monohydrate ($Cu(CH_3COO)_2 \cdot H_2O$, ≥98%), and zinc acetate dihydrate ($Zn(CH_3COO)_2 \cdot 2H_2O$, ≥99%) were used. All reagents were purchased from Sigma-Aldrich, Alfa Aesar, or equivalent suppliers and used as received without further purification. Ethanol, methanol, and deionized (DI) water were used as solvents throughout the process.

### 2.2. Fabrication of FTO/$TiO_2$/CdS/CdSe:Cu(0.3)/ZnS electrodes

The creation of the FTO/$TiO_2$/CdS/CdSe:Cu(0.3)/ZnS photoanode began with the formation of the FTO/$TiO_2$ film using the doctor blade technique and annealing at 500 °C for 1 h. Following this, the CdS layer is formed through the SILAR method, a process that involves placing the FTO/$TiO_2$ substrate in a 0.1 M cadmium ion ($Cd^{2+}$) solution for six minutes, rinsing with ethanol, and subsequently placing it in a 0.1 M sulfide ion ($S^{2-}$) solution for five minutes, and rinsing with methanol. This sequence was repeated thrice to ensure the creation of a consistent CdS layer. Subsequently, a CdSe:Cu(Cd:Cu = 0.3) layer was formed using the SILAR method. Initially, the Se precursor solution was prepared by dissolving 3.7812 g of sodium sulfite ($Na_2SO_4$) and 1.135 g of selenium powder in 50 mL of distilled water, followed by adding 2.5 milliliters of 1 mM sodium hydroxide (NaOH) to improve selenium solubility and agitating the mixture in a 70 °C oil bath for 16 h to produce a stable $Se^{2+}$ solution. A cadmium–copper solution was prepared by dissolving 0.0025572 g of CuCl and cadmium acetate in a 1 : 1 ethanol and water mixture. The FTO/$TiO_2$/CdS substrate was then immersed in this solution for five minutes, rinsed with ethanol, and dried in air. Next, the substrate was placed in a 70 °C $Se^{2+}$ solution for five minutes, cleaned with distilled water, and air-dried at room temperature. This process was performed three times to achieve controlled formation of the CdSe:Cu(0.3) layer. To enhance photostability and suppress surface recombination, a ZnS passivation layer was deposited

*via* 2 SILAR cycles using 0.1 M zinc acetate and 0.1 M sodium sulfide aqueous solutions.

### 2.3. Fabrication of QDSSCs with different counter electrodes

Counter electrodes were prepared using previously synthesized $Cu_4O_3$-*x* coated FTO substrates. The photoanode and counter electrode were assembled into a sandwich-type cell with a polysulfide electrolyte (0.5 M $Na_2S$, 2 M S, 0.2 M KCl in DI water/methanol, 3 : 7 v/v) introduced between the electrodes. The assembled QDSSCs were sealed and stored under ambient conditions for performance characterization.

### 2.4. Characterization

The optical characteristics of $Cu_4O_3$-*x* thin films were examined utilizing UV-vis spectroscopy (JASCO V-730) within the wavelength range of 190–1100 nm. Electrical conductivity measurements were conducted at 28 °C utilizing Hall effect measurement equipment (HL5500PC; Nanometrics Inc., USA). The elemental composition, comprising copper (Cu), oxygen (O), and nitrogen (N), was examined using X-ray spectroscopy through the energy-dispersive mechanism (EDX; FE-SEM; JEOL JSM-IT800). The films' morphology, including both the surface and cross-section, was examined utilizing FE-SEM. The binding energies of the elements were analyzed *via* X-ray photoelectron spectroscopy (XPS) using an AXIS Ultra DLD spectrometer (Kratos–Shimadzu) equipped with a monochromatic Al Kα X-ray source ($h\nu = 1486.6$ eV). The chamber pressure was maintained below $1 \times 10^{-8}$ torr during analysis. Survey spectra were collected over the binding energy range of 0–1350 eV with a pass energy of 160 eV and a step size of 1.0 eV to identify elemental composition. High-resolution spectra for core levels (*e.g.*, Cu 2p, O 1s, and N 1s) were acquired with a pass energy of 20 eV and a step size of 0.1 eV. The binding energy scale was calibrated using the adventitious C 1s peak at 284.8 eV. A Shirley background was subtracted, and the peak shapes were fitted using a Voigt function, which represents a convolution of Gaussian and Lorentzian components. The fitting parameters were carefully adjusted to minimize the residual error while maintaining physical relevance. Structural investigation was conducted *via* X-ray diffraction (XRD) utilizing a Shimadzu XRD-6100 instrument with Cu-Kα radiation. The rough surface with microscale features was assessed using microscopy based on the atomic force interaction mechanism (AFM; Bruker Dimension Edge). The electrochemical characteristics of the $Cu_4O_3$-*x*/FTO counter electrode were examined by spectroscopic impedance analysis and cyclic voltage measurement, employing a CHI 650E potentiostat/galvanostat. The redox electrolyte utilized in EIS studies consisted of 2 M $Na_2S$, 2 M elemental sulfur (S), and 0.2 M KCl. The counter electrode possessed an active area of 0.25 $cm^2$, with the inter-electrode distance between the counter and working electrodes regulated by using a set spacer. The current–voltage (*I–V*) properties of quantum dot-sensitized solar cells (QDSSCs) were assessed under light and dark conditions utilizing a solar simulator and a Keithley 2450 source meter. The light intensity was calibrated to 100 mW $cm^{-2}$ (AM 1.5G equivalent) using a silicon photodetector-based radiometer.

## 3. Results and discussion

### 3.1. Analysis of atomic composition *via* EDX

Nitrogen-doped $Cu_4O_3$ (denoted as $Cu_4O_3$-*x*) thin films were deposited on silicon substrates using a mixed gas containing varying ratios of $N_2$, in order to eliminate interference from oxygen originating from the glass substrate. This approach enables a more precise analysis of the elemental composition of Cu, O, and N within the films, providing a solid foundation for future research. The energy-dispersive X-ray spectroscopy (EDX) spectra of the $Cu_4O_3$-*x* films, shown in Fig. 1, exhibit characteristic $K_\alpha$ peaks for N and O at 0.39 keV and 0.52 keV, respectively, while the Cu $L_\alpha$ peak appears at 0.93 keV. Additionally, the Si $K_\alpha$ signal at 1.74 keV is observed, attributed to the Si substrate. The atomic compositions, summarized in Table 1, indicate an increase in N content with increasing *x*, which is correlated with a concurrent reduction in oxygen content. Here, the parameter *x* represents the increasing N fraction in the sputtering gas mixture. This trend suggests that N is substituting for O at lattice sites. Moreover, the atomic ratio $r = Cu/(N + O)$ is observed to decrease with increasing *x*, implying the formation of copper vacancies ($V_{Cu}$) within the lattice. The incorporation of N in place of O appears to promote the generation of these vacancies. The *r* value further supports the stoichiometric baseline of undoped copper oxide as $Cu_4O_3$. A declining *r* ratio with increasing N incorporation also suggests an evolution in the chemical environment, possibly indicating a shift in copper oxidation states or local bonding configurations. Moreover, the mapping images show the homogeneous distribution of all elements over the whole $Cu_4O_3$ films as seen in Fig. 2.

### 3.2. Analysis of atomic composition *via* XPS

XPS was utilized to provide a comprehensive understanding of the elemental composition and chemical states of N, O, and Cu in the $Cu_4O_3$-*x* thin films, using the C 1s peak at 284.8 eV as a reference. The corresponding spectra are shown in Fig. 3, with

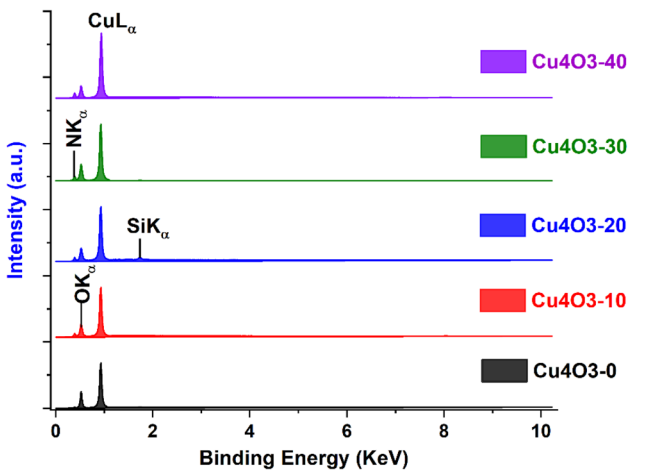


Fig. 1 EDX spectra of $Cu_4O_3$-*x* films deposited with varying $N_2$ contents in a mixed sputtering gas.

Table 1 The composition of $Cu_4O_3$-$x$ films determined by EDX spectra

| Samples | % at. Cu | % at. O | % at. N | Ratio of $\frac{Cu}{O+N}(r)$ |
|---|---|---|---|---|
| $Cu_4O_3$-0 | 59.57 | 40.03 | 0.4 | ≈1.47 |
| $Cu_4O_3$-10 | 58.54 | 38.91 | 2.55 | ≈1.41 |
| $Cu_4O_3$-20 | 57.71 | 39.01 | 3.28 | ≈1.36 |
| $Cu_4O_3$-30 | 56.92 | 38.65 | 4.43 | ≈1.32 |
| $Cu_4O_3$-40 | 55.85 | 37.83 | 6.32 | ≈1.27 |

Fig. 3A–C presenting the core-level binding energy profiles of N 1s, O 1s, and Cu 2p, respectively. As illustrated in Fig. 3A, the N 1s peak appears within the binding energy range of 393.3–398.8 eV, depending on the $x$ value. A noticeable shift toward lower binding energies is observed with increasing $x$, which is attributed to enhanced electronic screening effects as N becomes increasingly incorporated into the lattice. Fig. 3C displays the Cu 2p spectrum, characterized by a well-defined spin–orbit doublet corresponding to the $2p_{3/2}$ and $2p_{1/2}$ transitions, ranging from 932.7 to 952.7 eV. Notably, no significant shift in the Cu binding energies is detected as $x$ increases, suggesting that competing effects—namely electron withdrawal by N substituting for O or the reduction in oxygen vacancies, and electron donation associated with Cu vacancies effectively compensate for each other. This compensation maintains a relatively constant electron density around the Cu ions. To elucidate the oxidation states of Cu, the Cu $2p_{3/2}$ peak was deconvoluted into two distinct components corresponding to $Cu^{1+}$ and $Cu^{2+}$, located at 932.6 eV and 934.0 eV, respectively as reported in ref. 2, 3, 5 and 22. Fig. 3B shows the O 1s spectrum, which exhibits an asymmetric peak centered near 529.8 eV, indicating the presence of multiple oxygen species. Deconvolution reveals four components: (1) a peak at 529.8 eV assigned to lattice oxygen bonded to $Cu^{2+}$ ($O_{Cu2}$), (2) a peak at 530.4 eV corresponding to oxygen bound to $Cu^{1+}$ ($O_{Cu1}$), (3) a peak at

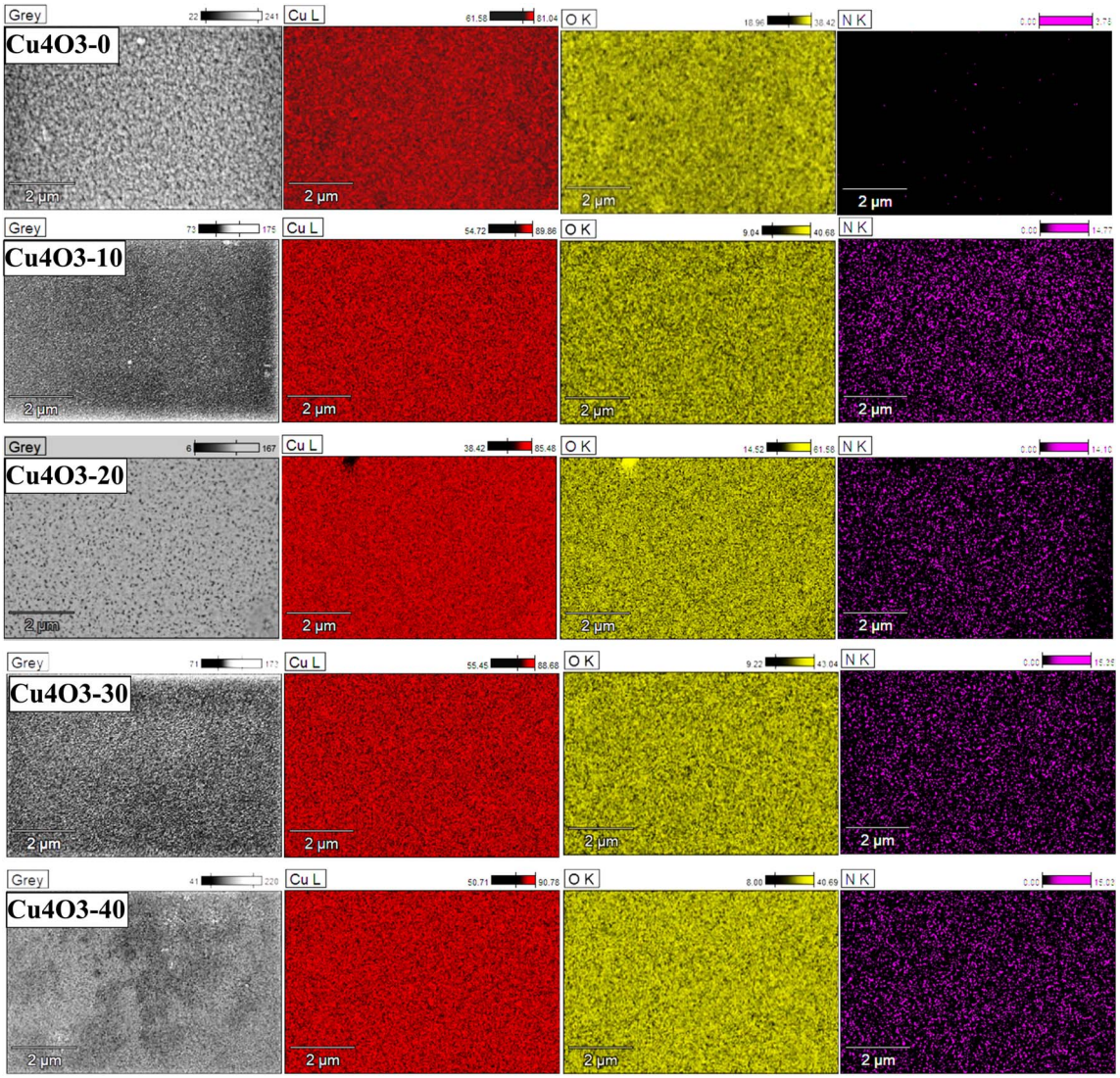


Fig. 2 EDX mapping images of $Cu_4O_3$-$x$ films deposited with varying $N_2$ contents in a mixed sputtering gas.

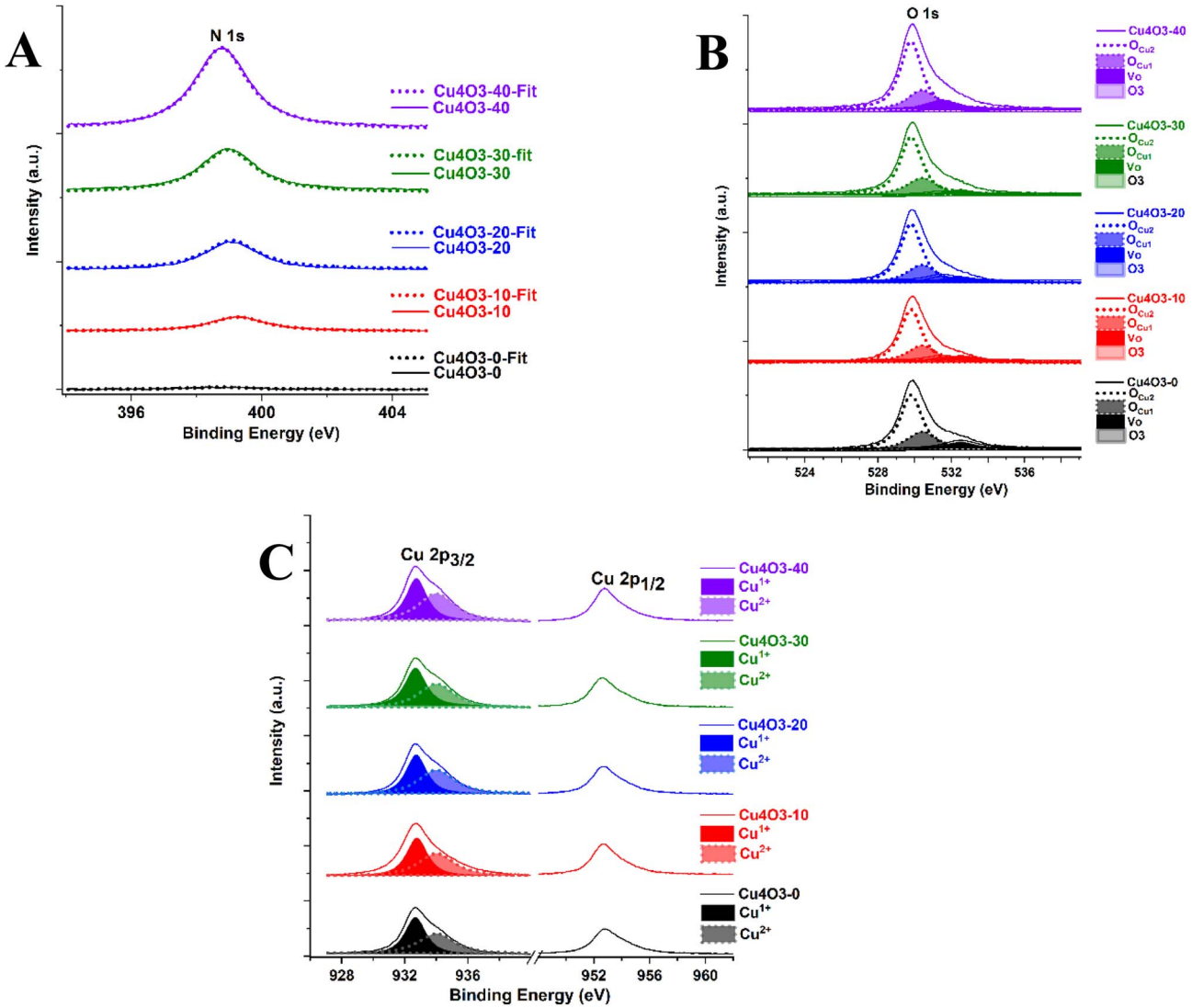


Fig. 3 XPS spectra of $Cu_4O_3$-*x* films deposited with varying $N_2$ contents in a mixed sputtering gas: (A) N 1s spectra, (B) O 1s spectra, and (C) Cu 2p spectra.

Table 2 The composition of $Cu_4O_3$-*x* films determined by XPS spectra

| Samples | $Cu_4O_3$-0 | $Cu_4O_3$-10 | $Cu_4O_3$-20 | $Cu_4O_3$-30 | $Cu_4O_3$-40 |
|---|---|---|---|---|---|
| % at. $Cu^{2+}$ | 28.03 | 28.68 | 28.99 | 29.18 | 29.19 |
| % at. $Cu^{1+}$ | 31.42 | 29.56 | 28.56 | 27.7 | 26.96 |
| % at. $Cu(Cu^{1+} + Cu^{2+})$ | 59.45 | 58.24 | 57.55 | 56.88 | 56.15 |
| % at. $O_{Cu2}$ | 23.76 | 24.45 | 24.84 | 25.15 | 24.59 |
| % at. $O_{Cu1}$ | 13.37 | 12.79 | 12.76 | 12.61 | 12.35 |
| % at. $V_O$ | 2.96 | 2.11 | 1.81 | 1.21 | 0.9 |
| % at. $O(O_1 + O_2 + V_O)$ | 40.09 | 39.35 | 39.41 | 38.97 | 37.84 |
| % at. N | 0.46 | 2.41 | 3.04 | 4.15 | 6.01 |
| Ratio of $\frac{Cu^{2+}}{Cu^{1+}}$ | ≈0.89 | ≈0.97 | ≈1.02 | ≈1.05 | ≈1.08 |
| Ratio of $\frac{O_{Cu2}}{O_{Cu1}}$ | ≈1.78 | ≈1.91 | ≈1.95 | ≈1.99 | ≈1.99 |
| Ratio of $\frac{Cu}{O+N}$ | ≈1.47 | ≈1.40 | ≈1.36 | ≈1.32 | ≈1.28 |

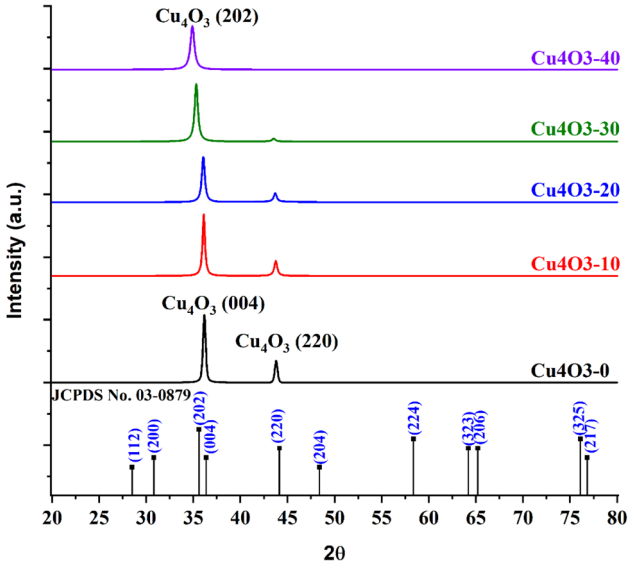


Fig. 4 XRD patterns of $Cu_4O_3$-$x$ films deposited with varying $N_2$ contents in a mixed sputtering gas.

531.0 eV attributed to $V_O$, and (4) a peak at 532.5 eV related to adsorbed oxygen species. These spectral features collectively demonstrate the evolution of chemical states with varying composition. The atomic percentage of each element (detailed in Table 2) was calculated using the integrated peak areas of the high-resolution XPS spectra and the corresponding atomic sensitivity factors (ASF) mentioned in ref. 35 ($S_{Cu2p_{3/2}} = 16.73$; $S_{O1s} = 2.93$; $S_{N1s} = 1.8$). The quantification follows the standard formula $N_i = \frac{\frac{I_i}{S_i}}{\sum \frac{I_j}{S_j}}$, where i and j represent Cu, N, and O, respectively. $I_{[i,j]}$ signifies the integrated intensity for element [i, j], whereas $S$[i, j] denotes the sensitivity factor. As $x$ increases, the N content increases while the O and $V_O$ contents decline, confirming that N atoms substitute for lattice O sites. Additionally, an increase in $Cu^{2+}$ content is evident with increasing $x$, as shown by the growing $Cu^{2+}/Cu^{+}$ ratio, which is consistent with the increase in the $O_{Cu2}$ component and the reduction in both $O_{Cu1}$ and $V_O$ contributions. Furthermore, Table 2 indicates that the atomic ratio of total Cu ($Cu^{+} + Cu^{2+}$) to the combined O and N content decreases from 1.47 to 1.28 with increasing $x$. This trend aligns with the nominal stoichiometry of $Cu_4O_3$ and reflects the overall reduction in Cu content relative to anion content due to N incorporation into the host lattice. Lastly, a comparison between XPS and EDX analyses reveals minor discrepancies in elemental ratios; however, the overall agreement supports the conclusion that the elemental distribution is homogeneous throughout thin films. In summary, XPS analysis confirms the substitution of O with N in $Cu_4O_3$, which intensifies with increasing $x$ and is linked to a decrease in $V_O$ and an increase in $V_{Cu}$, as seen by the increase in $Cu^{2+}$. The obtained results indicate the following expression for the Kröger–Vink doping reaction (eqn (1)):

$$\frac{1}{2}N_2(g) + V_O^{\cdot\cdot} + O_O^{\times} + 3Cu_{Cu}^{\times} \rightarrow N_O^{'} + 2Cu_{Cu}^{\cdot} + V_{Cu}^{'} + 2h^{\cdot} \quad (1)$$

Therein, $V_O^{\cdot\cdot}$ – represents an oxygen vacancy that is doubly positively charged; $O_O^{\times}$ denotes a neutral oxygen atom situated on an oxygen site; $Cu_{Cu}^{\times}$ – signifies a neutral copper atom located on a copper site; $Cu_{Cu}^{\cdot}$ – indicates a copper atom on a copper site with a positive effective charge ($Cu^{2+}$ or hole); $V_{Cu}^{'}$ – represents a negatively charged copper vacancy; $N_O^{'}$ – refers to a nitrogen atom substituting an oxygen site with a single negative charge; $h^{\cdot}$ – represents a hole; $\frac{1}{2}N_2(g)$ – denotes $N_2$ gas.

### 3.3. Analysis of structural properties with XRD patterns

The structural properties of $Cu_4O_3$-$x$ thin films were confirmed using X-ray diffraction (XRD) analysis, with reference to the standard JCPDS card no. 03-0879. For films deposited with N content up to $x \leq 20$, the diffraction pattern prominently exhibits the (004) lattice plane, accompanied by a weaker (220) peak (Fig. 4), indicating a preferential orientation along these planes. However, as the N incorporation increases to $x = 30$ and 40, the (004) reflection diminishes and is completely suppressed, while a new (202) peak emerges, suggesting a reorientation of the crystalline structure induced by higher N content. Additionally, the intensity of the (220) peak shows a consistent decline with increasing $x$, further evidencing structural modifications due to N doping. XRD peak positions for all films display a noticeable shift toward lower angles, as summarized in Table 3. This peak shift is indicative of lattice expansion, which strongly supports the successful substitution

Table 3 Structural parameters of $Cu_4O_3$-$x$ films deposited with varying $N_2$ contents in a mixed sputtering gas

| Samples | Lattice reflections of $Cu_4O_3$ | Diffractive angle $2\theta$ (degree) | Full width at half-maximum (degree) | Crystallite size $D$ (nm) | Weight percent of the phase | Average crystallite size $D$ (nm) | Lattice parameters (Å) |
|---|---|---|---|---|---|---|---|
| $Cu_4O_3$-0 | (004) | 36.16 | 0.30 | 27.87 | 0.7 | 28.07 | $c = 9.9332$ |
| | (220) | 43.78 | 0.30 | 28.55 | 0.3 | | $a = 5.8467$ |
| $Cu_4O_3$-10 | (004) | 36.10 | 0.30 | 27.86 | 0.77 | 26.78 | $c = 9.9491$ |
| | (220) | 43.74 | 0.37 | 23.15 | 0.23 | | $a = 5.8518$ |
| $Cu_4O_3$-20 | (004) | 36.04 | 0.39 | 21.43 | 0.47 | 21.71 | $c = 9.9652$ |
| | (220) | 43.68 | 0.39 | 21.95 | 0.53 | | $a = 5.8594$ |
| $Cu_4O_3$-30 | (202) | 35.30 | 0.41 | 20.34 | 0.98 | 20.26 | $c = 10.1298$ |
| | (220) | 43.54 | 0.53 | 16.15 | 0.02 | | $a = 5.8773$ |
| $Cu_4O_3$-40 | (202) | 34.90 | 0.49 | 17.00 | 1 | 17.00 | — |

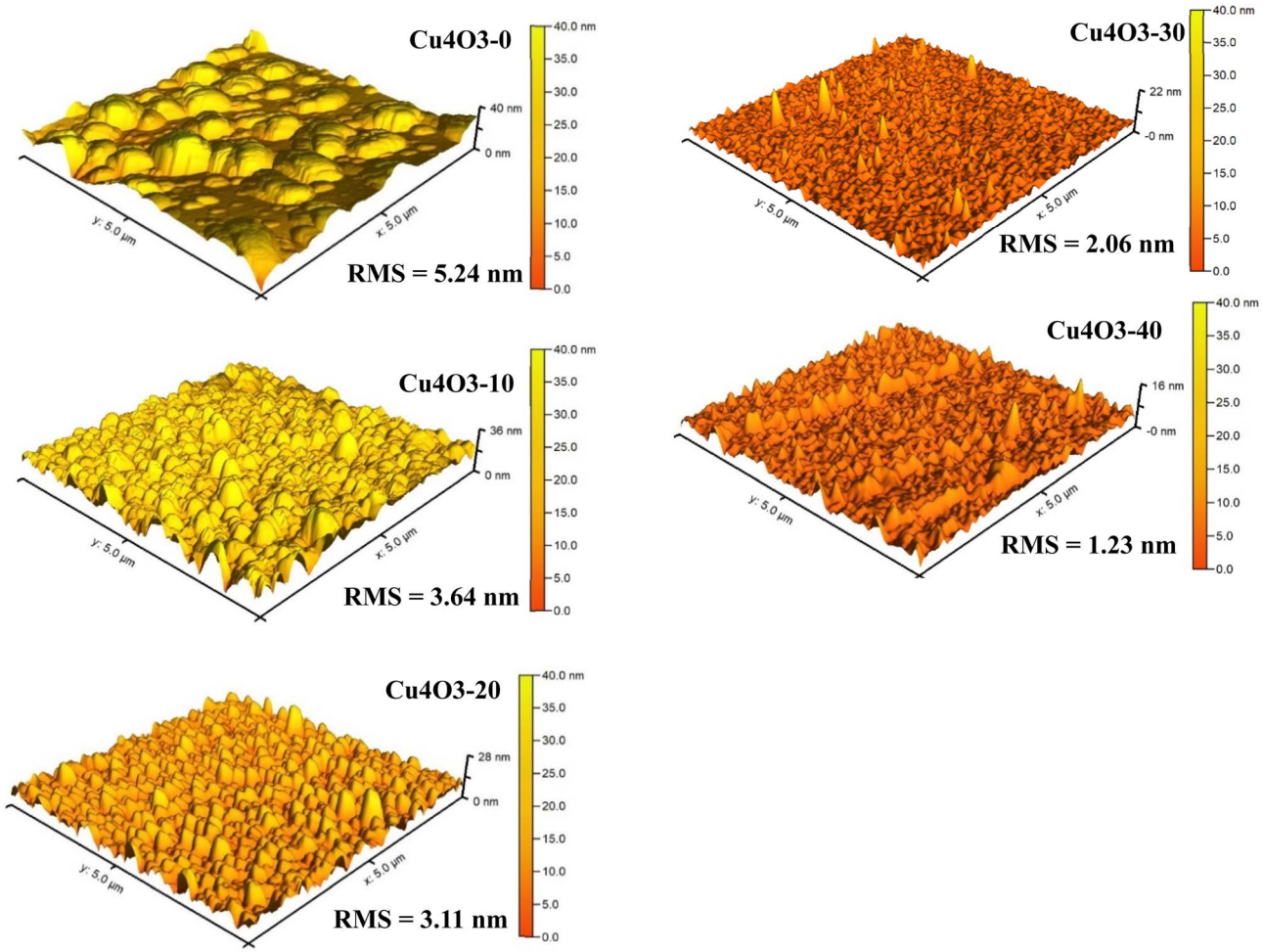


Fig. 5 AFM images of $Cu_4O_3$-$x$ films deposited with varying $N_2$ contents in a mixed sputtering gas.

of O atoms by N within the $Cu_4O_3$ crystal structure. Since $Cu_4O_3$ is an ionic crystal, the ionic radii of $N^{3-}$ (146 pm) and $O^{2-}$ (140 pm) should be considered. The substitution of smaller $O^{2-}$ ions by larger $N^{3-}$ ions leads to an increase in interplanar spacing, resulting in the observed diffraction peak shifts. Moreover, the average crystallite size, estimated using the Scherrer equation, decreases progressively with increasing N content. Despite this size reduction, the overall crystal quality of the films remains preserved, suggesting that N incorporation does not significantly deteriorate the crystal structure but instead alters the microstructure in a controlled manner. Correspondingly, the calculated lattice parameters $a$ and $c$ exhibit a monotonic increase with increasing $x$, further supporting the substitution of $O^{2-}$ by $N^{3-}$ ions in the $Cu_4O_3$ lattice and confirming the formation of an N-doped phase.

### 3.4. Analysis of morphology *via* AFM

The microscale surface morphology of $Cu_4O_3$-$x$ films, as observed by atomic force microscopy (AFM) in Fig. 5, indicates that the root mean square (RMS) surface roughness tends to decrease with increasing N content in the sputtering gas. However, this reduction in RMS does not correspond to better surface quality in all cases. For films deposited with $N_2$ concentrations up to 30%, both the RMS roughness and the surface grain distribution are favorable—smooth and uniform—making these films well-suited for interface-related applications. In contrast, the film produced at 40% $N_2$ exhibits inhomogeneous surface grain structures, despite having a lower RMS value. This inconsistency arises from N atoms substituting for O sites in the $Cu_4O_3$ lattice, which disturbs the microstructural development and leads to irregular surface grain growth. Therefore, among the tested conditions, the film deposited with 30% $N_2$ offers the best combination of surface smoothness and surface grain uniformity, making it the most appropriate choice for optoelectronic devices involving sensitive interfaces.

### 3.5. Analysis of morphology *via* FESEM

To comprehensively investigate the nanoscale morphology of the $Cu_4O_3$-$x$ thin films, FESEM analysis was performed, capturing both top-view and cross-sectional images as shown in Fig. 6. These images reveal a uniform grain distribution across the surface and through the cross-section of the films. The surface morphology of $Cu_4O_3$-$x$ films fabricated with N doping

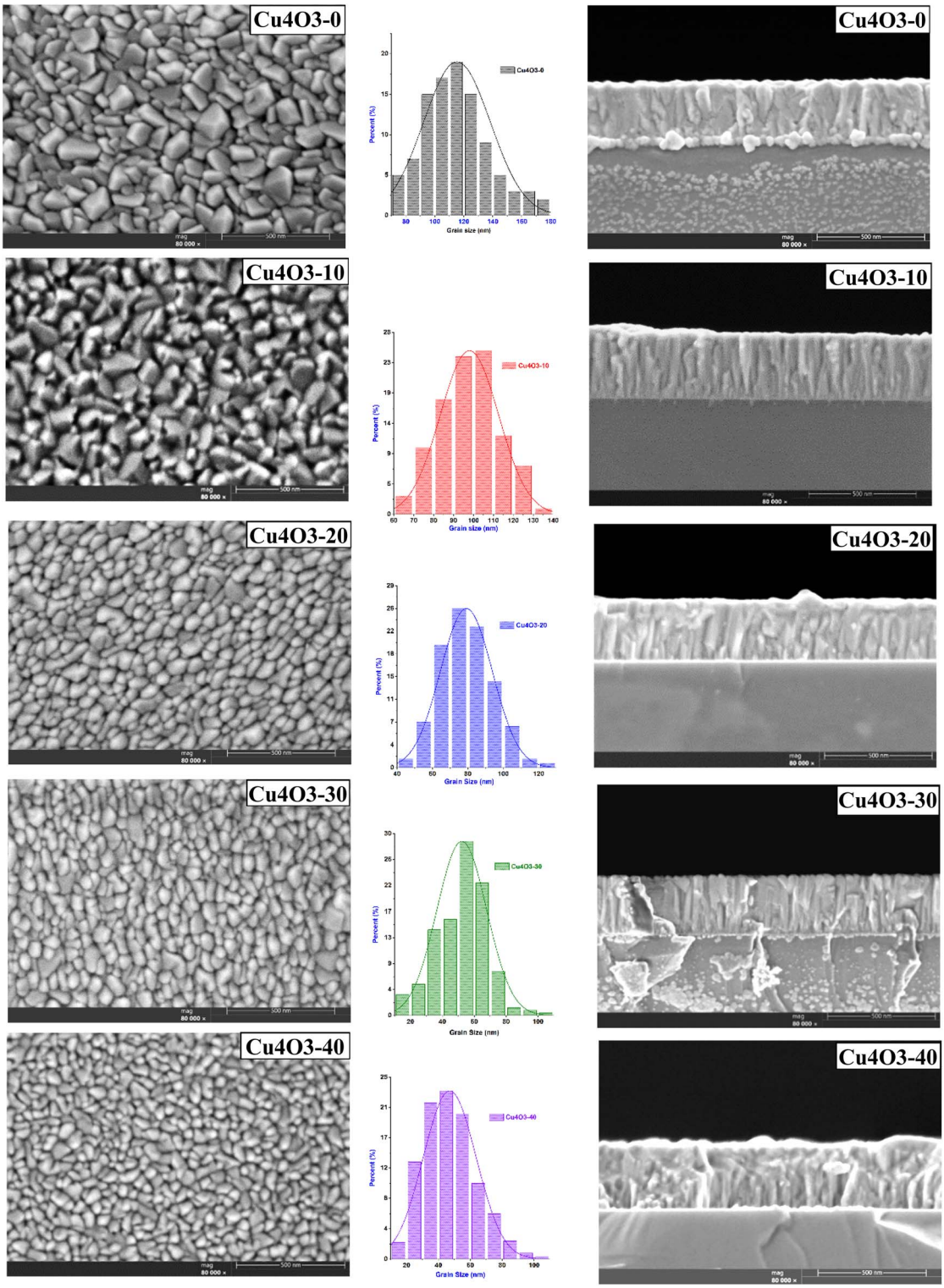


Fig. 6 FESEM images of $Cu_4O_3$-$x$ films deposited with the varying $N_2$ contents in a mixed sputtering gas.

levels from $x = 0$ to 10 displays a characteristic tetrahedral grain structure, marked by sharp angles and well-defined edges. As the $N_2$ concentration in the sputtering mixed gas increases ($x \geq 20$), there is a slight reduction in the sharpness of these angular features and edges; however, the overall grain shapes remain distinct and clearly defined, indicating that the crystalline integrity is largely preserved despite minor morphological smoothing. The cross-sectional FESEM images further reveal a well-developed columnar microstructure extending throughout the film thickness, mirroring the surface texture.

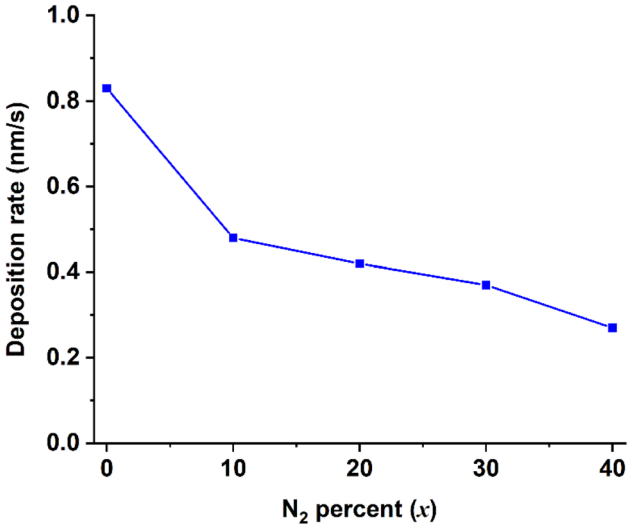


Fig. 7 Deposition rate of $Cu_4O_3$-$x$ with varying $N_2$ percent ($x$) in a mixed sputtering gas.

The $Cu_4O_3$-$x$ films were deposited with varying $N_2$ concentrations while maintaining a similar total thickness (~280–300 nm) by adjusting the deposition time. The deposition rate decreased with increasing $N_2$ content in the reactive atmosphere, from approximately 0.83 nm $s^{-1}$ at 0% $N_2$ to 0.27 nm $s^{-1}$ at 40% $N_2$ (Fig. 7). This reduction is attributed to target poisoning effects and changes in plasma chemistry under higher $N_2$ flow conditions. Additionally, a progressive decrease in grain size with increasing N content is observed, aligning with the crystallite size trends obtained from XRD analysis discussed in Section 3.3. Overall, the structural characterization by XRD, AFM, and FESEM collectively indicates that the $Cu_4O_3$-$x$ film fabricated at $x = 30$ exhibits an optimal combination of surface uniformity, low RMS, fine grain structure, and ordered columnar growth. This composition is particularly advantageous for applications requiring well-defined and stable interfacial features, such as in the integration of electrical or optoelectronic devices.

### 3.6. Analysis of optical characteristics utilizing UV-vis spectroscopy

In addition to the structural properties, it is crucial to investigate the optical behavior of $Cu_4O_3$-$x$ thin films in order to elucidate the influence of N incorporation on the electronic structure of the $Cu_4O_3$ lattice. UV-vis spectroscopy results, as presented in Fig. 8A, reveal that the films exhibit high optical transmittance, exceeding 70% across the visible spectrum. Notably, a red shift in the optical absorption edge is observed with increasing $x$, which signifies a progressive substitution of O atoms by N within the $Cu_4O_3$ lattice. This spectral shift is indicative of modifications in the electronic band structure, specifically due to the hybridization of N 2p orbitals with O 2p orbitals in the valence band. Such orbital mixing leads to an expansion of the valence bandwidth, thereby reducing the energy required for electronic transitions across the bandgap. This phenomenon is analogous to the band-edge shift mechanism previously reported for $Cu_2O$ systems, as described in ref. 36 and 37. To quantitatively evaluate the effect of N doping on the band structure, the optical bandgap values were determined using the Tauc method, assuming a direct allowed transition model in accordance with prior studies on $Cu_4O_3$ (ref. 38–41). The Tauc plots, shown in Fig. 8B, clearly illustrate a systematic narrowing of the bandgap with increasing N content (increasing $x$). This reduction in bandgap occurs because the N atoms interact more strongly with the O atoms in the material. Their electron energy levels mix together, which increases the energy of the valence band and makes it easier for electrons to jump to the conduction band, effectively lowering the bandgap.

### 3.7. Analysis of electrical characteristics by Hall measurements

As previously discussed, $Cu_4O_3$-$x$ thin films synthesized with varying N contents exhibit clear evidence of N atoms substituting

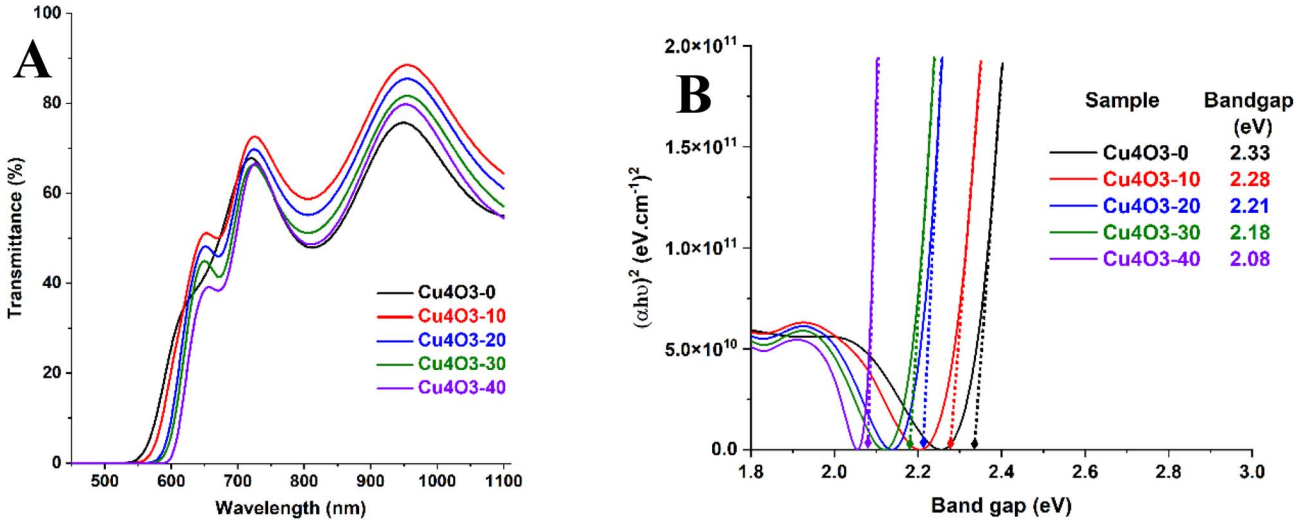


Fig. 8 (A) UV-vis transmittance spectra and (B) band gap of $Cu_4O_3$-$x$ films deposited with varying $N_2$ contents in a mixed sputtering gas.

Table 4 The results of the Hall effect measurement of $Cu_4O_3$-$x$ films deposited with varying $N_2$ contents in a mixed sputtering gas

| Samples | Electrical resistivity ($\rho$) ($\Omega$ cm) | Hall mobility ($\mu$) ($cm^2\ V^{-1}\ s^{-1}$) | Carrier concentration ($n$) ($cm^{-3}$) | Type |
|---|---|---|---|---|
| $Cu_4O_3$-0 | 64.07 | 7.26 | $1.34 \times 10^{16}$ | p |
| $Cu_4O_3$-10 | 9.3 | 6.83 | $9.84 \times 10^{16}$ | p |
| $Cu_4O_3$-20 | 6.63 | 4.55 | $2.07 \times 10^{17}$ | p |
| $Cu_4O_3$-30 | 4.19 | 4.48 | $3.33 \times 10^{17}$ | p |
| $Cu_4O_3$-40 | 5.68 | 2.04 | $5.39 \times 10^{17}$ | p |

for O within the lattice framework. This substitution leads to the formation of N-substituted O sites, which, in conjunction with intrinsic Cu vacancies, contribute to an increased hole concentration, as detailed in Table 4. However, despite the observed increase in hole concentration with increasing $x$, the overall electrical resistivity of the films does not continuously decrease. Instead, the minimum resistivity of 4.19 $\Omega$ cm is observed at $x =$ 30, beyond which resistivity increases. This non-monotonic behavior is primarily attributed to a pronounced reduction in hole mobility in the film with $x = 40$ (2.04 $cm^2\ V^{-1}\ s^{-1}$) relative to that with $x = 30$ (4.48 $cm^2\ V^{-1}\ s^{-1}$). The decline in mobility at higher N content may result from increased lattice disorder or scattering centers introduced by excessive N incorporation, which impedes efficient charge carrier transport.

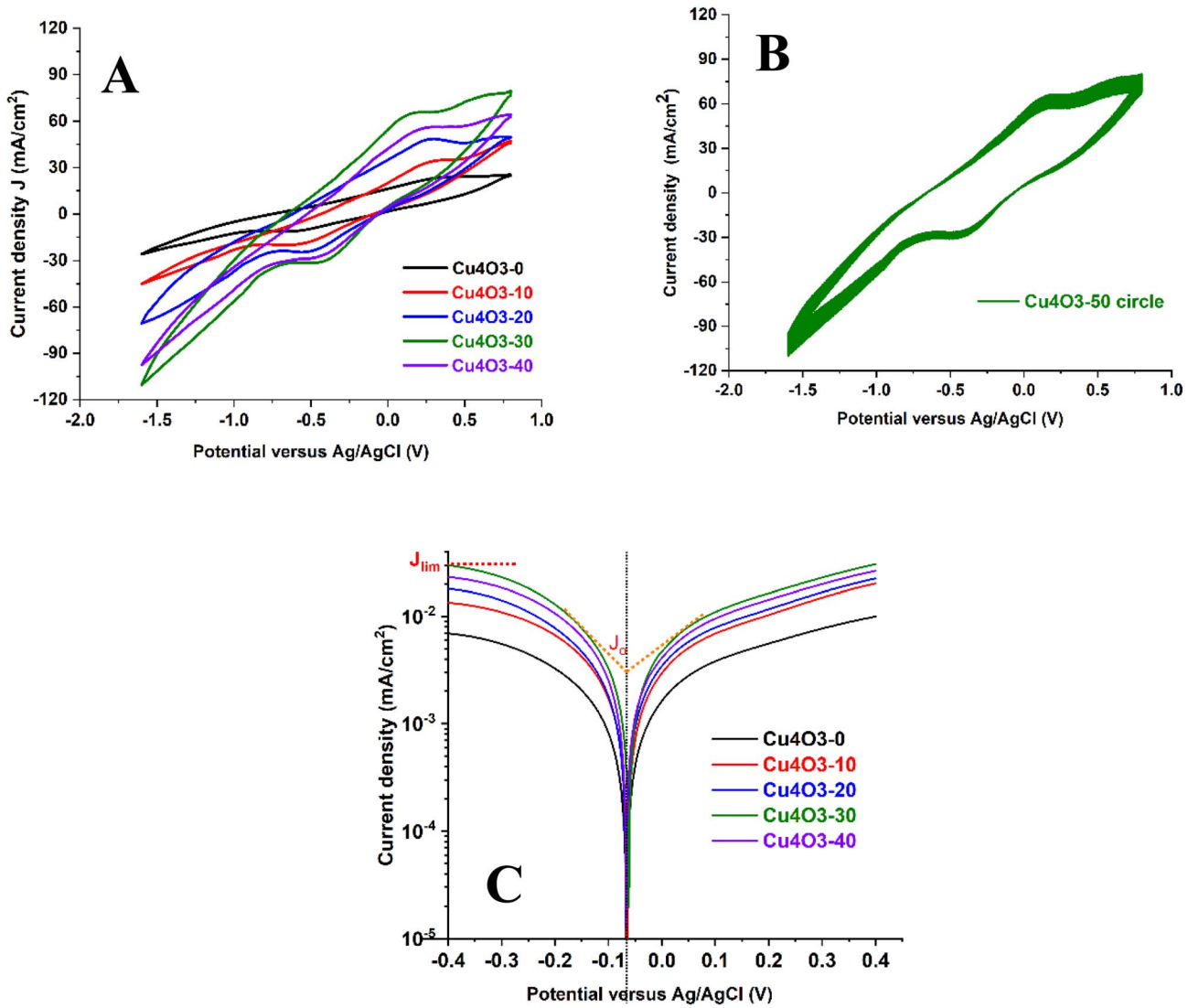


Fig. 9 (A) Cyclic voltammetry; (B) Tafel polarization of $Cu_4O_3$-$x$ films deposited with varying $N_2$ concentrations in a mixed sputtering gas; and (C) cyclic voltammetry of $Cu_4O_3$-30 film subjected to 50 cycles.

Table 5 Parameters of cyclic voltammetry and Tafel electrochemical characteristics of $Cu_4O_3$-*x*/FTO CE films with varying $N_2$ concentrations in a mixed sputtering gas

| Counter electrodes | $J_o(\times10^{-3})$ (mA cm$^{-2}$) | $J_{lim}(\times10^{-3})$ (mA cm$^{-2}$) | $J_{PC}$ (mA cm$^{-2}$) | $J_{PA}$ (mA cm$^{-2}$) | $\Delta V_{PP}$ (V) *versus* Ag/AgCl |
|---|---|---|---|---|---|
| $Cu_4O_3$-0/FTO | 2.3 | 6 | −11.07 | 24.38 | 0.90 |
| $Cu_4O_3$-10/FTO | 4.3 | 13 | −20.71 | 35.25 | 0.84 |
| $Cu_4O_3$-20/FTO | 5.1 | 18 | −25.74 | 49.44 | 0.76 |
| $Cu_4O_3$-30/FTO | 6.9 | 29 | −31.58 | 66.15 | 0.59 |
| $Cu_4O_3$-40/FTO | 5.6 | 23 | −28.18 | 56.10 | 0.69 |

### 3.8. Examination of the electrochemical properties of $Cu_4O_3$-*x* in a $Na_2S$ polysulfide electrolyte

To evaluate the charge carrier exchange dynamics between $Cu_4O_3$-*x* thin films and the $Sn^{2-}/S^{2-}$ redox couple, cyclic voltammetry (CV) measurements were performed over a potential range of −1.6 V to 0.8 V with a scan rate of 10 mV s$^{-1}$. As shown in Fig. 9A, all CV curves exhibit distinct anodic and cathodic peaks, confirming the occurrence of reversible charge transfer processes between the films and the electrolyte. The key electrochemical parameters extracted from the CV plots—including anodic and cathodic peak currents, anodic and cathodic peak voltages, and the peak-to-peak voltage separation ($\Delta V_{PP}$)—are summarized in Table 5. For films with *x* values from 0 to 30, both the anodic and cathodic currents, as well as the peak voltages, increase with increasing N content, while $\Delta V_{PP}$ exhibits a decreasing trend, suggesting enhanced electrochemical kinetics. Moreover, the film fabricated at $x = 30$ demonstrates the most favorable electrochemical performance, exhibiting the highest peak currents and the smallest $\Delta V_{PP}$, indicative of the most efficient charge transfer characteristics. Consistently, Tafel polarization measurements further corroborate this observation: the film with $x = 30$ achieves the highest limited current density ($J_{lim}$) of 29 × 10$^{-3}$ mA cm$^{-2}$ and exchange current density ($J_0$) of 6.9 × 10$^{-3}$ mA cm$^{-2}$ as seen in Fig. 9C. These results imply that the $Cu_4O_3$-30 film possesses

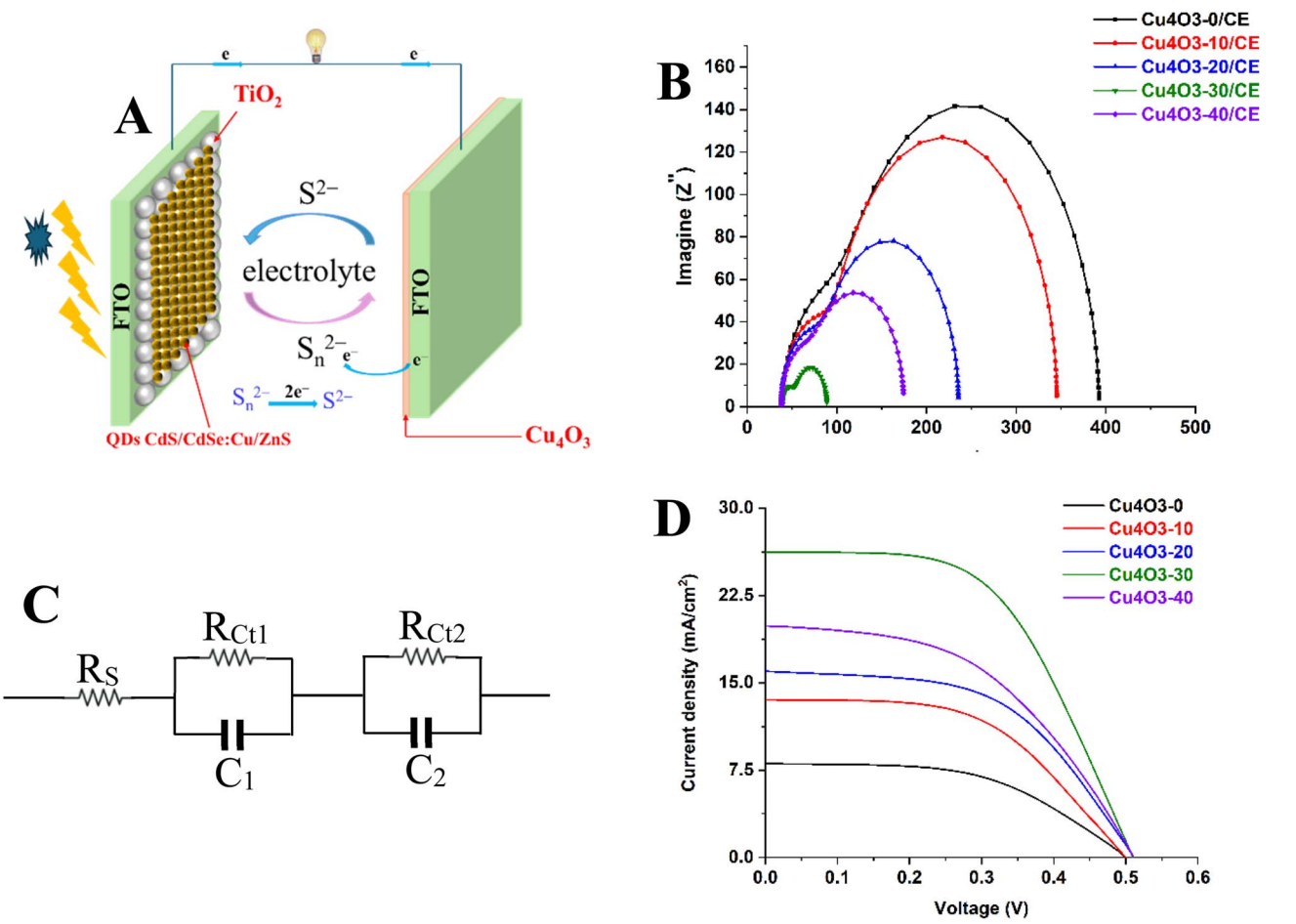


Fig. 10 (A) Diagram of solar cells; (B) Nyquist plots (C) the equivalent circuit; (D) *J*–*V* curves.

Table 6 Parameters of EIS electrochemical characteristics and solar cell efficiency based on $Cu_4O_3$-$x$/FTO CE films with different $N_2$ contents in a mixed sputtering gas

| Sample | Open voltage ($V_{oc}$, V) | Short current density ($J_{sc}$, mA cm$^{-2}$) | Fill factor (FF) | Efficiency ($\eta$, %) | $R_s$ (Ω) | $R_{ct1}$ (Ω) | $R_{ct2}$ (Ω) |
|---|---|---|---|---|---|---|---|
| $Cu_4O_3$-0 | 0.50 | 8.05 | 0.52 | ∼2.09 | 38.16 | 284.7 | 70.04 |
| $Cu_4O_3$-10 | 0.50 | 13.57 | 0.53 | ∼3.60 | 38.58 | 248.9 | 58.12 |
| $Cu_4O_3$-20 | 0.51 | 15.98 | 0.53 | ∼4.32 | 38.77 | 150.3 | 48.23 |
| $Cu_4O_3$-30 | 0.51 | 25.51 | 0.56 | ∼7.29 | 38.90 | 34.9 | 15.14 |
| $Cu_4O_3$-40 | 0.51 | 19.88 | 0.51 | ∼5.17 | 38.86 | 99.4 | 36.42 |

Table 7 Photovoltaic performance of the $Cu_4O_3$-30 counter electrode compared with various $Cu_2S$/$Cu_xS$-based CEs in QDSSCs

| CE/source | Photoanode structure | $J_{sc}$ (mA cm$^{-2}$) | $V_{oc}$ (V) | FF (%) | $\eta$ (%) | References |
|---|---|---|---|---|---|---|
| $Cu_4O_3$ | FTO/$TiO_2$/CdS/CdSe/ZnS | 25.51 | 0.51 | 56.0 | 7.29 | This work |
| $Cu_2S$ (electrodeposited) | FTO/$TiO_2$/CdS/CdSe | 19.60 | 0.45 | 48.62 | 4.24 | 42 |
| $Cu_2S$ (bare) | FTO/$TiO_2$/CdS/CdSe | 15.84 | 0.56 | 50.07 | 4.35 | 42 |
| $Cu_2S$/PbS (3 SILAR cycles) | FTO/$TiO_2$/CdS/CdSe/PbS | 18.08 | 0.55 | 53.55 | 5.28 | 43 |
| ATO/CuS | ATO/$TiO_2$/CdS/CdSe | 20.22 | 0.57 | 41.49 | 4.79 | 44 |
| ATO/PbSe | ATO/$TiO_2$/CdS/CdSe/PbSe | 17.18 | 0.59 | 55.06 | 5.59 | 45 |
| $Cu_2S$/$Cu_2Se$ composite | FTO/$TiO_2$/CdS/CdSe | 19.18 | — | — | 4.60 | 46 |
| $CuInS_2$–$Cu_2S$ nanocomposite | FTO/$TiO_2$/CdS/CdSe | 4.74 | 0.73 | 58.0 | 2.01 | 47 |
| Se-doped CuS | FTO/$TiO_2$/CdS/CdSe | 6.74 | 0.37 | 67.10 | 1.68 | 48 |

superior catalytic activity toward polysulfide redox reactions. Furthermore, it facilitates the most efficient diffusion of polysulfide species at the counter electrode (CE)/electrolyte interface, underscoring its potential as an effective CE material for polysulfide-based electrochemical systems. This is confirmed further by the CV plot (Fig. 9B) of $Cu_4O_3$-30 with 50 cycles which shows a weak current decreasing trend of 0.015 mA cm$^{-2}$.

### 3.9. EIS spectra and *J–V* characteristics of CdS/CdSe:Cu/ZnS QDSSCs with $Cu_4O_3$-$x$ CEs

A schematic of the quantum dot-sensitized solar cell (QDSSC) structure, designed specifically to investigate electrochemical impedance spectroscopy (EIS) and current–voltage (*J–V*) characteristics, is illustrated in Fig. 10A. These devices are configured as $TiO_2$/CdS/CdSe:Cu/ZnS/QDSSCs employing $Cu_4O_3$-$x$ counter electrodes (CEs). The fabrication methodology for the $TiO_2$/CdS/CdSe:Cu/ZnS photoanodes closely follows the procedures detailed in ref. 32. The Nyquist plots obtained from EIS measurements, presented in Fig. 10B, reveal two distinct semicircles for all tested devices. The appearance of two semicircles is attributed to two separate interfacial processes: the smaller high-frequency semicircle corresponds to the charge transfer resistance at the CE/electrolyte interface, while the larger mid-frequency semicircle originates from charge recombination processes at the photoanode. Based on these observations, appropriate equivalent circuit models were developed and are shown in Fig. 10C. Key electrochemical parameters were extracted by fitting the EIS data using Autolab software, with the results summarized in Table 6. In this analysis, the resistance $R_{ct2}$ represents the charge transfer resistance at the CE/electrolyte interface, directly reflecting the catalytic activity of the counter electrode. In contrast, $R_{ct1}$ corresponds to the resistance associated with electron recombination at the $TiO_2$/quantum dot (QD) interface. The principal emphasis of this study is the efficacy of counter electrodes, with particular attention devoted to the fluctuation of $R_{ct2}$ values. The results indicate that the $Cu_4O_3$-30 counter electrode exhibits the lowest $R_{ct2}$ value among all samples, signifying the most efficient and reversible electrochemical charge transfer process. Interestingly, a similar trend is observed for $R_{ct1}$, despite the identical fabrication conditions for all QD photoanodes, suggesting a synergistic improvement possibly related to the overall interfacial properties of the device. Overall, the $Cu_4O_3$-30 counter electrode's better electrochemical performance, as evidenced by cyclic voltammetry (CV), Tafel polarization, and Nyquist analyses, directly correlates with the highest photovoltaic efficiency of 7.29% observed for the solar cells utilizing the $Cu_4O_3$-30 CE, as summarized in Table 6 and shown in Fig. 10D. This confirms the critical role of optimized $Cu_4O_3$-30 counter electrodes in enhancing the performance of polysulfide-based QDSSCs. The optimized $Cu_4O_3$-30 CE in this work delivers a PCE of 7.29%, surpassing most reported $Cu_2S$/$Cu_xS$-based counterparts (1.68–5.59%) in comparable device architectures as seen in Table 7, owing to its superior electrocatalytic activity and lower charge-transfer resistance. We attribute the enhanced performance to the unique morphology and optoelectronic characteristics of the $Cu_4O_3$ films, including improved light absorption and interfacial charge transfer.

## 4. Conclusion

$Cu_4O_3$-$x$ thin films were successfully deposited under varying nitrogen ($N_2$) concentrations in the sputtering gas mixture to

systematically optimize their structural, optical, and electrical properties. Among the fabricated samples, the $Cu_4O_3$-30 film, synthesized with 30% $N_2$ in the sputtering atmosphere, exhibited the most favorable characteristics. This film demonstrated an optimal balance between crystallinity and morphology, with an average crystallite size of approximately 20 nm, a surface roughness (RMS) of 2.06 nm, and a grain size of about 50 nm as observed by FESEM. In terms of optical properties, the $Cu_4O_3$-30 film possessed a direct optical bandgap of 2.18 eV. Regarding electrical performance, it achieved a resistivity of 4.19 Ω cm, a hole concentration of $3.33 \times 10^{17}$ $cm^{-3}$, and a hole mobility of 4.48 $cm^2 V^{-1} s^{-1}$. Leveraging these superior properties, the $Cu_4O_3$-30 film was employed as a CE material in CdS/CdSe:Cu/ZnS/$TiO_2$ quantum dot-sensitized solar cells (QDSSCs). The resulting devices exhibited a remarkable power conversion efficiency (PCE) of 7.29%, primarily ascribed to the superior catalytic performance and effective charge transfer at the CE/electrolyte interaction. Notably, this efficiency surpasses that of comparable QDSSCs utilizing conventional $Cu_2S$ counter electrodes, highlighting the significant potential of optimized $Cu_4O_3$-*x* films for high-performance photovoltaic applications.

## Conflicts of interest

There are no conflicts to declare.

## Data availability

All data relevant for the reproduction of the results presented in this work are included within the article.

## Acknowledgements

This research is funded by Vietnam National University, Ho Chi Minh City (VNU-HCM) under grant number C2025-18-08.

## References

1 W. Maeng, S.-H. Lee, J.-D. Kwon, J. Park and J.-S. Park, Atomic layer deposited p-type copper oxide thin films and the associated thin film transistor properties, *Ceram. Int.*, 2016, **42**, 5517–5522.
2 A. Lakshmanan, Z. C. Alex and S. R. Meher, $Cu_2O$ thin films grown by magnetron sputtering as solar cell absorber layers, *Mater. Sci. Semicond. Process.*, 2022, **148**, 106818.
3 F. Yang, W. Peng, Y. Zhou, R. Li, G. Xiang, J. Z. YueLiu, J. Zhang, Y. Zhao and H. Wang, Thermal optimization of defected $Cu_2O$ photon-absorbing layer and the steady p-$Cu_2O$/n-Si photovoltaic application, *Vacuum*, 2022, **198**, 110876.
4 J.-S. Yoon, J.-W. Lee and Y.-M. Sung, Enhanced photoelectrochemical properties of Z-scheme ZnO/p–n $Cu_2O$ PV-PEC cells, *J. Alloys Compd.*, 2019, **771**, 869–876.
5 M. R. Dustgeer, S. T. Asma, A. Jilani, K. Raza, S. Z. Hussain, M. B. Shakoor, J. Iqbal, M. Sh. Abdel-wahab and R. Darwesh, Synthesis and characterization of a novel single-phase sputtered $Cu_2O$ thin films: Structural, antibacterial activity and photocatalytic degradation of methylene blue, *Inorg. Chem. Commun.*, 2021, **128**, 108606.
6 X. Wu, J. Liu, P. Huang, Z. Huang, F. Lai, G. Chen, L. Lin, P. Lv, W. Zheng and Y. Qu, Engineering crystal orientation of p-$Cu_2O$ on heterojunction solar cells, *Surf. Eng.*, 2017, **33**, 542–547.
7 S. Aseena, N. Abraham, G. Sahaya Dennish Babu, S. Kathiresan and V. Suresh Babu, Solution-Synthesized $Cu_2O$ As a Hole Transport Layer for a ZnO-Based Planar Heterojunction Perovskite Solar Cell Fabricated at Room Temperature, *J. Electron. Mater.*, 2022, **51**, 1692–1699.
8 D. Prasanth, K. P. Sibin and H. C. Barshilia, Optical properties of sputter deposited nanocrystalline CuO thin films, *Thin Solid Films*, 2019, **673**, 78–85.
9 H. Güney, D. İskenderoğlu, M. E. Güldüren, K. Ç. Demİr and S. M. Karadeniz, An investigation on CuO thin films grown by ultrasonic spray pyrolysis at different substrate temperatures: Structural, optical and supercapacitor electrode characterizations, *Opt. Mater.*, 2022, **132**, 112869.
10 P. Venkateswari, P. Thirunavukkarasu, M. Ramamurthy, M. Balaji and J. Chandrasekaran, Optimization and characterization of CuO thin films for P–N junction diode application by JNSP technique, *Optik*, 2017, **140**, 476–484.
11 A. H. Shukor, H. A. Alhattab and I. Takano, Electrical and optical properties of copper oxide thin films prepared by DC magnetron sputtering, *J. Vac. Sci. Technol., B: Nanotechnol. Microelectron.: Mater., Process., Meas., Phenom.*, 2020, **38**, 012803.
12 Y. Akaltun, Effect of thickness on the structural and optical properties of CuO thin films grown by successive ionic layer adsorption and reaction, *Thin Solid Films*, 2015, **594**, 30–34.
13 L. Radjehi, L. Aissani, A. Djelloul, S. Lamri, K. Nomenyo, S. Achache, G. Lerondel and F. Sanchette, Effect of vacuum annealing on the structural and optical properties of sputtered $Cu_4O_3$ thin films, *Surf. Eng.*, 2021, **37**, 422–428.
14 M. A. M. Patwary, C. Y. Ho, K. Saito, Q. Guo, K. M. Yu, W. Walukiewicz and T. Tanaka, Effect of oxygen flow rate on properties of $Cu_4O_3$ thin films fabricated by radio frequency magnetron sputtering, *J. Appl. Phys.*, 2020, **127**, 085302.
15 M. A. M. Patwary, K. Saito, Q. Guo, T. Tanaka, K. Man Yu and W. Walukiewicz, Nitrogen Doping Effect in $Cu_4O_3$ Thin Films Fabricated by Radio Frequency Magnetron Sputtering, *Phys. Status Solidi B*, 2020, **257**, 1900363.
16 D. S. Murali and A. Subrahmanyam, Synthesis of low resistive p type $Cu_4O_3$ thin films by DC reactive magnetron sputtering and conversion of $Cu_4O_3$ into CuO by laser irradiation, *J. Phys. D: Appl. Phys.*, 2016, **49**, 375102.
17 L. Yang, R. Wang, D. Chu, Z. Chen, F. Zhong, X. Xu, C. Deng, H. Yu and J. Lv, $BiVO_4$ photoelectrodes for unbiased solar water splitting devices enabled by electrodepositing of $Cu_2O$ simultaneously as photoanode and photocathode, *J. Alloys Compd.*, 2023, **945**, 169336.

18 Y. Wang, N. Yu and Y. Wu, $Cu_2O$/GaN ultraviolet detector synthesized using ZnO nanorod arrays as template by aqueous method, *Nano-Struct. Nano-Objects*, 2020, **23**, 100494.
19 T. Minami, H. Tanaka, T. Shimakawa, T. Miyata and H. Sato, High-Efficiency Oxide Heterojunction Solar Cells Using $Cu_2O$ Sheets, *Jpn. J. Appl. Phys.*, 2004, **43**, L917.
20 T. Minami, Y. Nishi and T. Miyata, Efficiency enhancement using a $Zn_{1-x}Ge_x$-O thin film as an n-type window layer in $Cu_2O$ -based heterojunction solar cells, *Appl. Phys. Express*, 2016, **9**, 052301.
21 D.-C. Perng, M.-H. Hong, K.-H. Chen and K.-H. Chen, Enhancement of short-circuit current density in $Cu_2O$/ZnO heterojunction solar cells, *J. Alloys Compd.*, 2017, **695**, 549–554.
22 Y. Liu, J. Zhu, L. Cai, Z. Yao, C. Duan, Z. Zhao, C. Zhao and W. Mai, Solution-Processed High-Quality $Cu_2O$ Thin Films as Hole Transport Layers for Pushing the Conversion Efficiency Limit of $Cu_2O$/Si Heterojunction Solar Cells, *Sol. RRL*, 2020, **4**, 1900339.
23 K. Eom, D. Lee, S. Kim and H. Seo, Modified band alignment effect in ZnO/$Cu_2O$ heterojunction solar cells via $Cs_2O$ buffer insertion, *J. Phys. D: Appl. Phys.*, 2018, **51**, 055101.
24 V. S. Nguyen, A. Sekkat, D. Bellet, G. Chichignoud, A. Kaminski-Cachopo, D. Muñoz-Rojas and W. Favre, Open-air, low-temperature deposition of phase pure $Cu_2O$ thin films as efficient hole-transporting layers for silicon heterojunction solar cells, *J. Mater. Chem. A*, 2021, **9**, 15968–15974.
25 C. Qin, Y. Wang, Z. Lou, S. Yue, W. Niu and L. Zhu, Surface modification and stoichiometry control of $Cu_2O/SnO_2$ heterojunction solar cell by an ultrathin MgO tunneling layer, *J. Alloys Compd.*, 2019, **779**, 387–393.
26 T. Minami, Y. Nishi and T. Miyata, $Cu_2O$-based solar cells using oxide semiconductors, *J. Semicond.*, 2016, **37**, 014002.
27 T. Minami, Y. Nishi and T. Miyata, Heterojunction solar cell with 6% efficiency based on an n-type aluminum–gallium–oxide thin film and p-type sodium-doped $Cu_2O$ sheet, *Appl. Phys. Express*, 2015, **8**, 022301.
28 K. Sahu, A. Bisht, S. A. Khan, I. Sulania, R. Singhal, A. Pandey and S. Mohapatra, Thickness dependent optical, structural, morphological, photocatalytic and catalytic properties of radio frequency magnetron sputtered nanostructured $Cu_2O$–CuO thin films, *Ceram. Int.*, 2020, **46**, 14902–14912.
29 H.-H. Zeng, A. S. Rasal, M. Alemayehu Abate, A. Vithal Ghule and J.-Y. Chang, Surface and interfacial engineering for aqueous-processed quantum dots-sensitized solar cell with efficiency approaching 11%, *Chem. Eng. J.*, 2024, **495**, 153702.
30 L. G. Tartuci, E. Raphael, J. A. Carvalho Junior, W. S. Machado and M. A. Schiavon, Counter Electrodes Based on Polyaniline/carbon Nanotube/$Cu_xS$ Nanocomposites for CdS Quantum Dots-Sensitized Solar Cells, *Energ. Tech.*, 2025, 2402251.
31 Z. Luo, W. Yin, J. Wang, Y. Hua, Z. Zhou, W. Zhang, S. Chen, X. Zhang and W. Zheng, Quantum Dots Enable Perovskite Solar Cells Performance: Interactions, Mechanisms, Progresses, and Future Perspectives, *Adv. Funct. Mater.*, 2025, **35**, 2419268.
32 D. H. Phuc and H. T. Tung, Quantum dot sensitized solar cell based on the different photoelectrodes for the enhanced performance, *Sol. Energy Mater. Sol. Cells*, 2019, **196**, 78–83.
33 K. Zhao, H. Yu, H. Zhang and X. Zhong, Electroplating Cuprous Sulfide Counter Electrode for High-Efficiency Long-Term Stability Quantum Dot Sensitized Solar Cells, *J. Phys. Chem. C*, 2014, **118**, 5683–5690.
34 E. J. Radich, R. Dwyer and P. V. Kamat, $Cu_2S$ Reduced Graphene Oxide Composite for High-Efficiency Quantum Dot Solar Cells. Overcoming the Redox Limitations of $S^{2-}$/$S_n^{2-}$ at the Counter Electrode, *J. Phys. Chem. Lett.*, 2011, **2**, 2453–2460.
35 B. V. Crist, *Handbooks of Monochromatic XPS Spectra – the Elements and Native Oxides*, XPS Inter-national LLC, Mountain View (CA, USA), 1999, vol. 1.
36 S. Hassaballa, A. Aljabri, S. H. Mohamed, A. M. Bakry, A. M. A. El-Rahman and M. A. Awad, Photocatalysis, wettability and optical properties of N-doped $Cu_2O$/CuO thin films for smart coating applications, *Phys. Scr.*, 2024, **99**, 115974.
37 M. Li, J.-Y. Zhang, Y. Zhang and T.-M. Wang, Oxygen vacancy in N-doped $Cu_2O$ crystals: A density functional theory study, *Chin. Phys. B*, 2012, **21**, 087301.
38 A. Thobor and J. F. Pierson, Properties and air annealing of paramelaconite thin films, *Mater. Lett.*, 2003, **57**, 3676–3680.
39 J. F. Pierson, D. Wiederkehr and A. Billard, Reactive magnetron sputtering of copper, silver, and gold, *Thin Solid Films*, 2005, **478**, 196–205.
40 J. F. Pierson, A. Thobor-Keck and A. Billard, Cuprite, paramelaconite and tenorite films deposited by reactive magnetron sputtering, *Appl. Surf. Sci.*, 2003, **210**, 359–367.
41 J. F. Pierson, E. Duverger and O. Banakh, Experimental and theoretical contributions to the determination of optical properties of synthetic paramelaconite, *J. Solid State Chem.*, 2007, **180**, 968–973.
42 J. Wang, M. M. Rahman, C. Ge and J.-J. Lee, Electrodeposition of $Cu_2S$ nanoparticles on fluorine-doped tin oxide for efficient counter electrode of quantum-dot-sensitized solar cells, *J. Ind. Eng. Chem.*, 2018, **62**, 185–191.
43 I.-R. Jo, J. A. Rajesh, Y.-H. Lee, J.-H. Park and K.-S. Ahn, Enhanced electrocatalytic activity and electrochemical stability of $Cu_2S$/PbS counter electrode for quantum-dot-sensitized solar cells, *Appl. Surf. Sci.*, 2020, **525**, 146643.
44 L. Zhou, H. L. Ren, C. Q. Yang, Y. X. Wu and B. B. Jin, ATO/CuS composite counter electrodes enhanced the photovoltaic performance of quantum dot sensitized solar cells, *Inorg. Chem. Commun.*, 2022, **138**, 109273.
45 B. B. Jin, H. S. Huang, S. Y. Kong, G. Q. Zhang, B. Yang, C. X. Jiang, Y. Zhou, D. J. Wang and J. H. Zeng, Antimony tin oxide/lead selenide composite as efficient counter electrode material for quantum dot-sensitized solar cells, *J. Colloid Interface Sci.*, 2021, **598**, 492–499.
46 Y. Chen, D. Wang, Y. Lin, X. Zou and T. Xie, An in situ inward etching strategy for constructing a p-p heterojunction $Cu_2S$/

$Cu_{2-x}Se$ material based on brass as an effective counter electrode for quantum dot sensitized solar cells, *J. Power Sources*, 2019, **442**, 227222.

47 M. Mousavi-Kamazani, Z. Salehi and K. Motevalli, Enhancement of quantum dot-sensitized solar cells performance using $CuInS_2$–$Cu_2S$ nanocomposite synthesized by a green method, *Appl. Phys. A*, 2017, **123**, 691.

48 G. Vinoth, S. Abinaya and M. R. Kadiresan, Hydrothermal Synthesis of Se-Doped CuS Quantum Dots with Respect to the DW/EN Solvent Ratio and Application as a Counter Electrode for Quantum Dot-Sensitized Solar Cells, *Braz. J. Phys.*, 2023, **53**, 1.